

Article

Analysis of Aerodynamic Noise Characteristics of High-Speed Train Pantograph with Different Installation Bases

Yongfang Yao ^{1,2}, Zhenxu Sun ^{1,*} , Guowei Yang ^{1,2}, Wen Liu ³ and Prasert Prapamonthon ^{1,4}

¹ Key Laboratory for Mechanics in Fluid Solid Coupling Systems, Institute of Mechanics, Chinese Academy of Sciences, Beijing 100190, China; yaoyongfang@imech.ac.cn (Y.Y.); gwyang@imech.ac.cn (G.Y.); prasert.pr@kmitl.ac.th (P.P.)

² School of Engineering Sciences, University of Chinese Academy of Sciences, Beijing 100190, China

³ Industrial Software (Beijing) Co., Ltd., Beijing 100101, China; wenliu@siemens.com

⁴ International Academy of Aviation Industry, King Mongkut's Institute of Technology Ladkrabang, Bangkok 10520, Thailand

* Correspondence: sunzhenxu@imech.ac.cn; Tel.: +86-10-82543815

Received: 22 April 2019; Accepted: 4 June 2019; Published: 6 June 2019



Abstract: The high-speed-train pantograph is a complex structure that consists of different rod-shaped and rectangular surfaces. Flow phenomena around the pantograph are complicated and can cause a large proportion of aerodynamic noise, which is one of the main aerodynamic noise sources of a high-speed train. Therefore, better understanding of aerodynamic noise characteristics is needed. In this study, the large eddy simulation (LES) coupled with the acoustic finite element method (FEM) is applied to analyze aerodynamic noise characteristics of a high-speed train with a pantograph installed on different configurations of the roof base, i.e. flush and sunken surfaces. Numerical results are presented in terms of acoustic pressure spectra and distributions of aerodynamic noise in near-field and far-field regions under up- and down-pantograph as well as flushed and sunken pantograph base conditions. The results show that the pantograph with the sunken base configuration provides better aerodynamic noise performances when compared to that with the flush base configuration. The noise induced by the down-pantograph is higher than that by the up-pantograph under the same condition under the pantograph shape and opening direction selected in this paper. The results also indicate that, in general, the directivity of the noise induced by the down-pantograph with sunken base configuration is slighter than that with the flush configuration. However, for the up-pantograph, the directivity is close to each other in Y-Z or X-Z plane whether it is under flush or sunken roof base condition. However, the sunken installation is still conducive to the noise environment on both sides of the track.

Keywords: high-speed train; pantograph; aerodynamic noise; large eddy simulation; acoustic finite element method

1. Introduction

Over the last twenty years, high-speed trains have played a major role in community and urban development. It is well known that, as the speed of a high-speed train increases, aerodynamic problems that can be neglected at low speeds become more serious. For such cases, the problem of aerodynamic noise cannot be avoided and must be addressed. Therefore, better understanding of the aerodynamic noise characteristics is needed. To alleviate the aerodynamic noise problems, the shape of complex parts is optimized and appropriate sound barriers are commonly used. Presently, a large number of high-speed trains can reach an operating speed of about 300–350 km/h. With these speeds, the

trains cause serious aerodynamic noise pollution to passengers and surroundings. Zhang [1] indicated that aerodynamic noise becomes a main pollution source when train speed exceeds 250–300 km/h. His results indicated that, with the increase of train speed, the noise increases rapidly and the aerodynamic noise almost increases with the sixth power of the train speed. To date, the aerodynamic noise characteristics of high-speed trains have been investigated numerically and experimentally. Based on numerical approaches, aero-acoustic analysis is applied to simplified and real-oriented high-speed train geometries to evaluate aerodynamic noise. The numerical approaches could be divided into direct and hybrid methods. The direct methods commonly use the direct numerical simulation (DNS), large eddy simulation (LES), or detached eddy simulation (DES) to simulate the flow field and aerodynamic noise simultaneously. In this kind of methods, the grid scale and energy capture requirements differ between the analysis of the flow field and the analysis of the acoustic propagation. It is found that the magnitude of sound pressure is smaller when compared to that of the dynamic pressure in the flow field. The direct methods are required to adopt high-order, low-dissipation, low-dispersion discretization schemes to produce appropriately accurate solutions [2]. Moreover, since the shape of high-speed trains is rather complex, the use of the direct methods can suffer from high computational costs. Consequently, the hybrid methods seem at present more attractive for practical engineering problems. In the hybrid methods, sound sources in the near field and sound propagation in the far field are solved separately. The pressure fluctuations are solved using a high-order technique of LES, DES or are modeled from turbulence statistics obtained from Reynolds Average Navier-Stokes (RANS) simulations. Then, the pressure fluctuations are analyzed by means of acoustic methods to solve the acoustic propagation. Presently, the trend of the research on the aerodynamic noise of high-speed trains is mostly based on the hybrid methods.

On simplified train geometries, it is found that effects of flow separation and vortices from the head, the tail, and the car connections are the main sources of aerodynamic noise. Sun et al. [3] studied the near-field and far-field aerodynamic noise characteristics and comprehensively assessed the noise level of the key parts in a simplified CRH3 high-speed train model using the Non-Linear Acoustic method (NLAS) and the Ffowcs Williams–Hawkings (FW-H) acoustic analogy approach. Their results indicated that the head and the tail are the main noise sources. In addition, the results indicated that the rough areas with cavities or hump faces on the train structure contribute significantly to the aerodynamic noise. Moreover, it was found that the car connection area is also a noise source. Liu et al. [4] used unsteady incompressible flow analysis to obtain the fluctuation pressure on the train surface, and the FW-H method was adopted to predict the noise propagation to the far field. They studied the spectral characteristics of the head surface of a simplified high-speed train, and the aerodynamic noise sources and the aerodynamic noise distribution in the far-field region. Their results revealed that aerodynamic noise could be greatly reduced as long as the shapes of train head and body are optimized. Aerodynamic noise of more realistic high-speed geometries has been investigated by including more complicated components, such as pantographs and bogies. It was observed by Zhu and Jing [5], and Sun et al. [6] that the aerodynamic noise sources come from the pantographs, the bogies, the car head, and the rear of the car. Previously, King et al. [7] showed that the correlation between the logarithm of the aerodynamic noise and the running speed of the pantograph is approximately linear. Takaishi et al. [8,9] used LES and the compact Green's function to simulate the distribution of the dipole noise source on the bogie and the surface of the pantograph. Their results showed that periodic vortices induced by unstable shear layer separation at the leading edge of the bogie section in the flow provide the major part of sound generation [8]. Furthermore, Takaishi et al. [9] indicated that the dipole sound sources around the pantograph make a strong aerodynamic noise source due to the fact that the dipole sound sources are formed strongly in the shear layer close to the model surface. Yoshiki et al. [10] used the Lattice Boltzmann Method (LBM) to calculate the aerodynamic noise of the pantograph, and numerical results gave good agreement with the experimental results obtained by wind tunnel test. Liu [11] used LES to simulate the unsteady incompressible flow on the pantograph, and the far-field aerodynamic noise of pantograph was calculated by Lighthill's acoustic

analogy. The characteristics of sound pressure level, frequency spectrum and the relationship between sound pressure level and speed was investigated. It was found that the sound pressure level increases significantly with the increase of vehicle speed and is approximately linear with the logarithm of vehicle speed. Tan and Xie [12] used LES, the scale adaptive simulation (SAS), the improved delayed detached eddy simulation with shear-stress transport $k-\omega$ (IDDES SST $k-\omega$), the delayed detached eddy simulation with shear-stress transport $k-\omega$ (DDES SST $k-\omega$), and the delayed detached eddy simulation with realizable $k-\varepsilon$ (DDES Realizable $k-\varepsilon$) models to investigate the flow-field structures, the aeroacoustic sources, and the aeroacoustics of pantographs. By means of a hybrid method of NLAS and FW-H acoustic analogy, Yu et al. [13] studied the aerodynamic noise of the pantograph system, specifically to predict the influence of the pantograph covers on noise in the speed range. Besides the methods used to conduct acoustic propagation as mentioned above, there are still other methods for universal acoustic propagation calculations such as the acoustic boundary element method (BEM) and the acoustic finite element method (FEM). CFD transient simulation is used to obtain the fluctuating pressure in the time domain on the boundary of the pantograph, and is transformed into the frequency domain to form the boundary conditions of the acoustic finite element to further solve the far-field noise. By means of the combined CFD/FW-H the acoustic analogy with BEM, aerodynamic noise from a pantograph was predicted by Sun et al. [14] and by Zhang et al. [15]. According to Zhang et al. [15], they used LES with high-order finite difference schemes to analyze the near-field unsteady flow around the pantograph, while the far-field aerodynamic noise was predicted using the CFD/FW-H acoustic analogy. The results of the surface pressure fluctuations were used in BEM to predict aerodynamic noise sources of the pantograph and the far-field sound radiation. The results showed that the aerodynamic noise originates mainly from the top regions of the pantograph rather than from the bottom regions. Also, the results indicated that the noise generated from the pantograph oriented opposite to the direction to the motion is lower than that oriented in the same direction to the motion, by as much as 3.4 dB(A). Sun et al. [14] used DES to analyze the flow field. They also used BEM to predict the aerodynamic noise from a pantograph, giving the spatial and spectral characteristics of the noise around the pantograph. Several previous experiments also showed evidence that the pantograph is an important component that generates high intensity of noise. For example, Kitagawa and Nagakura [16,17] showed that the main road-side noise is the aerodynamic noise produced by the pantograph and bogie. Noger et al. [18] tested a 1/7th scaled train model with and without pantograph in a wind tunnel and showed that the space near the rear vertical face of the cavity is the most complex and turbulent region. This is the origin of the most important noise generation. Their research suggested that the modification of the cavity geometry with passive devices or active control can be an effective method for reducing the radiated noise. Lawson and Barakos [19] indicated that the length/height ratio of the cavity has a greater impact on its internal flow field, which then also affects pantograph noise. However, the spatial distribution and directivity of far-field noise in the experiment was not discussed deeply in their work. Hence, the influence on noise from the cavity needs to be further explored.

Overall, few studies on the effects of the installation base configuration of the pantograph on the aerodynamic noise characteristics have been done so far. In fact, the flow field of a high-speed train can be seriously disturbed by non-flush surfaces of the train body and then complex flow separation and vortex shedding are caused. This disturbance leads to fluctuating surface pressure that becomes a significant aerodynamic noise source, which radiates to far field regions. The mechanism of aero-acoustic propagation and aerodynamic noise physical characteristics caused by complex structures such as the pantograph and the bogies remain challenging and need to be further discussed. The objective of the present work is to numerically investigate the effects of the pantograph with different installation bases of a high-speed train on the aerodynamic and on the acoustic characteristics using LES with the acoustic FEM. The spectral characteristics and directivity of the aerodynamic noise are discussed. This work can provide high-speed train designers and investigators with useful knowledge of the aerodynamic noise characteristics under different configurations of the installation base of the pantograph.

2. Computational Models

The pantograph used in the present study consists of insulators, chassis, upper arm, lower arm rod and double slide, as depicted in Figure 1. The upper arm and lower arm rod can move vertically, and are controlled by the base frame mechanism. On the roof of the train body, the pantograph is installed, either flush or sunken. Namely, the flush surface configuration of the roof is used as the baseline for a comparison with the sunken surface configuration. Scenarios of the up and down pantograph with the different configurations of the pantograph installation on the surface roof are shown in Figure 2.

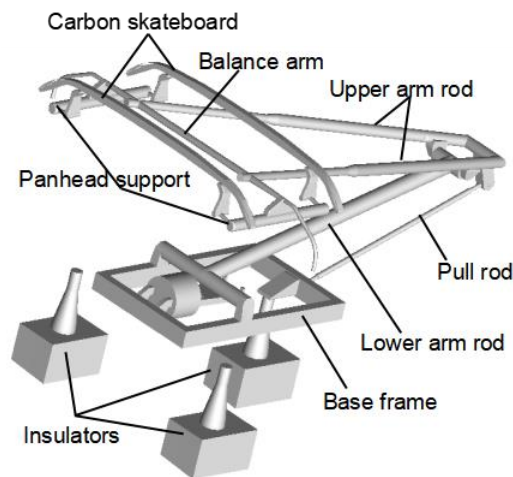


Figure 1. Model of pantograph.

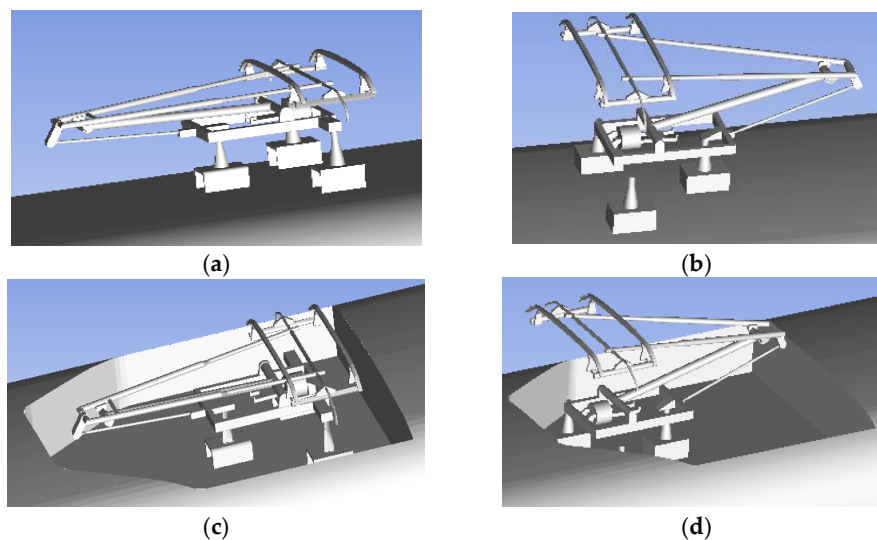


Figure 2. Scenarios of pantograph with different configurations of installation base: (a) model of down-pantograph with flush installation; (b) model of up-pantograph with flush installation; (c) model of down-pantograph with sunken installation; and (d) model of up-pantograph with sunken installation.

3. Computational Methods

The commercial CFD program STAR-CCM+, which is based on the finite-volume method, is used to simulate the flow field around the pantograph and the installation base. The LES method is used to conduct the dynamic flow characteristics, including the fluctuating pressure on the pantograph and the base. Then, the fluctuating pressure in the time domain is transformed into the frequency domain by the Fast Fourier Transform (FFT) method and the acoustic FEM with commercial program LMS Virtual lab is used to evaluate the acoustic noise of radiation from the pantograph.

3.1. Large Eddy Simulation

According to LES, the large-scale eddies in a fully turbulent flow are computed directly and the influence of the small eddies on the large-scale eddies is modeled. The continuity equation and the Favre averaged compressible Navier–Stokes equations, as expressed mathematically in Equations (1) and (2), respectively, are solved implicitly.

$$\frac{\partial \rho}{\partial t} + \frac{\partial}{\partial x_i}(\rho \bar{u}_i) = 0 \tag{1}$$

$$\frac{\partial}{\partial t}(\rho \bar{u}_i) + \frac{\partial}{\partial x_i}(\rho \bar{u}_i \bar{u}_j) = \frac{\partial}{\partial x_j}(\sigma_{i,j}) - \frac{\partial \bar{p}}{\partial x_i} - \frac{\partial \tau_{i,j}}{\partial x_j} \tag{2}$$

where $\sigma_{i,j}$ and $\tau_{i,j}$ are defined as Equations (3) and (4), respectively.

$$\sigma_{i,j} = [\mu(\frac{\partial \bar{u}_i}{\partial x_j} + \frac{\partial \bar{u}_j}{\partial x_i})] - \frac{2}{3}\mu \frac{\partial \bar{u}_i}{\partial x_j} \delta_{i,j} \tag{3}$$

$$\tau_{i,j} = \rho \overline{u_i u_j} - \bar{\rho} \bar{u}_i \bar{u}_j \tag{4}$$

where \bar{u}_i is the resolved filtered velocity vector, $\sigma_{i,j}$ is the stress tensor caused by molecular viscosity, and $\tau_{i,j}$ is the sub-grid scale (SGS) stress tensor, representing the diffusive effect of the sub-grid scale eddies on the resolved ones. The Smagorinsky model [20] is used to model the SGS stresses because of its simplicity.

3.2. Acoustic Finite Element Method

The acoustic FEM is used to compute the sound pressure level (SPL). This method can take the reflection effect of the car body structure surface on the noise [21] into consideration. The acoustic FEM procedure starts from calculating the noise propagation from the Helmholtz equation as defined in Equation (5):

$$\nabla^2 \cdot p(x, y, z) + k^2 p(x, y, z) = f(x, y, z) \tag{5}$$

where $p(x, y, z)$ is the acoustic pressure, $k = 2\pi f/c$ is the wave-number, and f is the frequency. The corresponding wavelength is computed from Equation (6):

$$\lambda = 2\pi/k = 2\pi c/\omega = c/f \tag{6}$$

where c is the free-stream speed of sound. Then, the FFT method is adopted for spectral analysis. The square of the amplitude of pressure wave is expressed in terms of the summation of sine and cosine functions, as shown in Equation (7):

$$A^2(\omega_k) = 2 \left[\frac{1}{N} \sum_{n=1}^{N-1} (p_n - \bar{p}) \cos\left[\frac{2\pi nk}{N}\right] \right]^2 + 2 \left[\frac{1}{N} \sum_{n=1}^{N-1} (p_n - \bar{p}) \sin\left[\frac{2\pi nk}{N}\right] \right]^2 \tag{7}$$

where P_n is a data set and represents the fluctuating pressure of the N th step; $n = 0, \dots, N - 1$. Meanwhile, $\omega_k = k/N\delta t$, where δt is the time step. Finally, the SPL is computed by Equation (8).

$$SPL(\omega_k) = 10 \log(A^2/P_{ref}^2) \tag{8}$$

where P_{ref} is constant and equal to 2×10^{-5} Pa.

3.3. Computational Domain and Boundary Conditions

The computation domain is depicted in Figure 3. The flow field is tested to confirm that it is large enough to eliminate boundary effects. The computational domain size is $96.5H \times 45H \times 20H$, where H is the height of the train and $H = 3.55$ m. The origin of the Cartesian reference system locates at the distance $x = 29$ m from the train geometry. The inflow velocity is 350 km/h. The Reynolds number, Re , is 2.25×10^7 based on inflow velocity and the train's height H . A three-car train model with the pantograph is used to study the effects of the pantograph with different configurations of the installation base on the aerodynamic noise characteristics. The effects of other complicated components, such as bogies and windshields, are neglected to save computational cost.

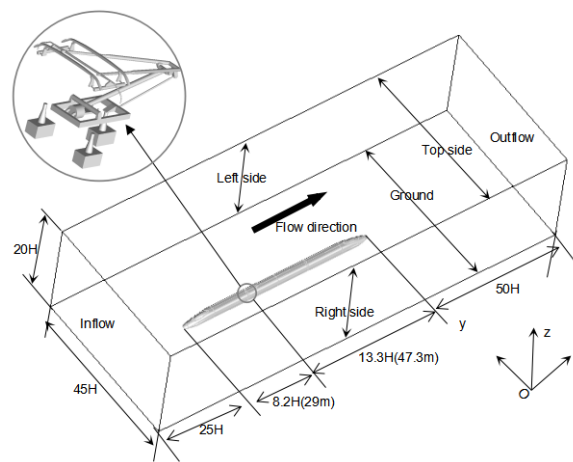


Figure 3. Computational domain for flow field and aerodynamic noise.

The physical time step of the calculation is 10^{-4} s and 20 sub-steps are used within each time step. The total physical calculation time is 0.4 s. The Courant–Friedrichs–Lewy number ($CFL = u\Delta t/\Delta x$) is less than 1 so that the calculation is converged within each time step. Boundary conditions are set as follows: (1) The surface of the train is a fixed wall with non-slip and penetration conditions. (2) Both lateral sides and the top of the computational domain are given as the far field condition with the characteristic line method, and the air flows in the positive x -direction. (3) The ground is set to be a moving wall, and its velocity is the same as the incoming velocity of the air. Figure 4 shows the observer locations used to evaluate the acoustic pressure spectrum and directivity in the near and far field of the pantograph, namely, two positions at $y = 5$ and 25 m for the spectrum characteristics, and planes $y = 0, 10$ and 20 m for the distributions of aerodynamic noise, respectively. Furthermore, five positions in the x -direction i.e. $x = 0, 5, 10, 15$ and 20 m are monitored to investigate the overall sound pressure level (OASPL) caused by the pantograph with the different base configurations. It should be noted that these five positions are 3.5 m above the ground.

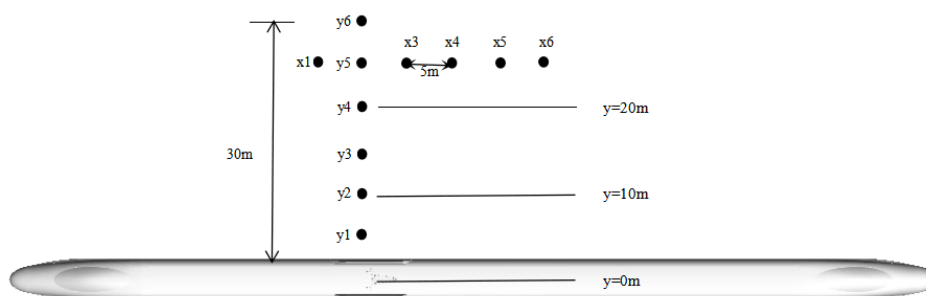


Figure 4. Locations of aerodynamic noise observers.

3.4. Mesh Strategy

The STAR-CCM+ mesher is used to generate the computational grids. On the grid arrangement of flow field computation domain, the first layer thickness is 0.05 mm, the geometric grid growth rate is 1.1, and the number of the grid layers close to the train surface is 10 to resolve flow in the boundary layer. The grid size on the pantograph surface and train body surface is 10 mm and 60 mm, respectively, and mesh refinement rear the train body and pantograph is employed to make the computational grid fine enough to capture flow field physics. An isotropic mesh is used in the whole flow field except near wall boundaries. Three sets of grids, i.e., coarse, medium and fine grids, are used to test the grid sensitivity of the simulations. The total number of grid cells in the three grid configurations are 15, 30 and 60 million cells, respectively. Four mesh refinement zones including small, middle, big and wake region are set up, as shown in Figure 5. The mesh size of each refinement zone is listed in Table 1.

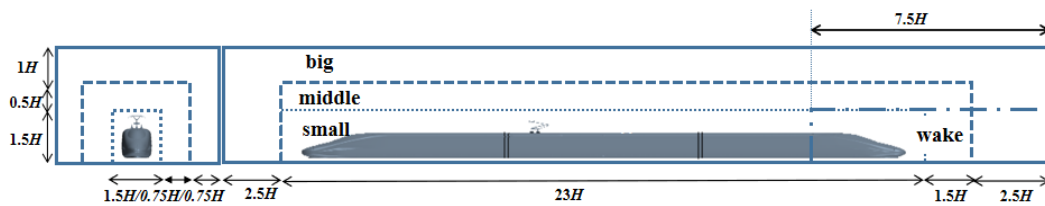


Figure 5. The distribution of refinement zone.

Table 1. The mesh size of the refinement zone.

Grids	Coarse	Medium	Fine
Grid size settings (mm) (small, middle, big, wake)	18, 18, 36, 9	8, 12, 24, 6	6, 9, 18, 6
Total numbers	15 million	30 million	60 million

Figure 6 shows the distribution of time-averaged slipstream velocity along a sampling line at a distance of 2 m from the center of the train, 1.3 m above the ground predicted by the coarse, medium and fine meshes. The non-dimensional results of slipstream velocity U_{non} is defined as:

$$U_{non} = \sqrt{(V_x - V_\infty)^2 + V_y^2 + V_z^2} / V_\infty \quad (9)$$

where V_x , V_y and V_z are the velocity components along the x-direction, y-direction and z-direction, respectively, as shown in Figure 3.

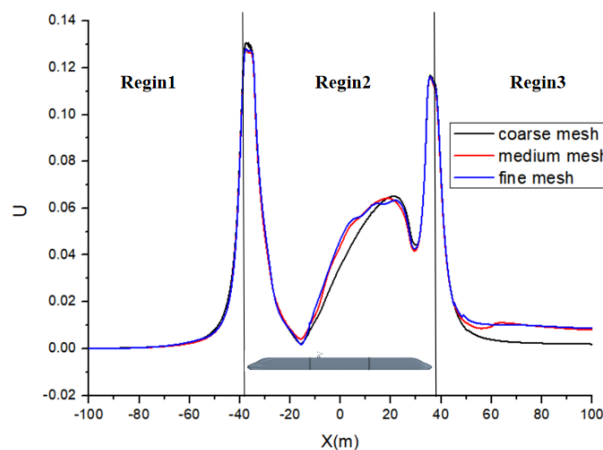


Figure 6. The distribution non-dimensional time-averaged slipstream velocity.

Figure 6 shows that the time-averaged non-dimensional slipstream velocity shows larger difference between the coarse and the fine meshes near the train in Region 2 and in the wake propagation Region 3, indicating that the coarse mesh is inadequate analytical accuracy, while the medium mesh exhibits good consistence with the fine mesh. Thus, the medium grid configuration is adopted to calculate characteristics of flow field, as it gives a satisfactory balance between accuracy and computational costs. Figure 7 shows the medium grids around the train surfaces. Because pantograph noise is the main research content, the area near the pantograph is refined. The total number of the computational cells used is about 32 million.

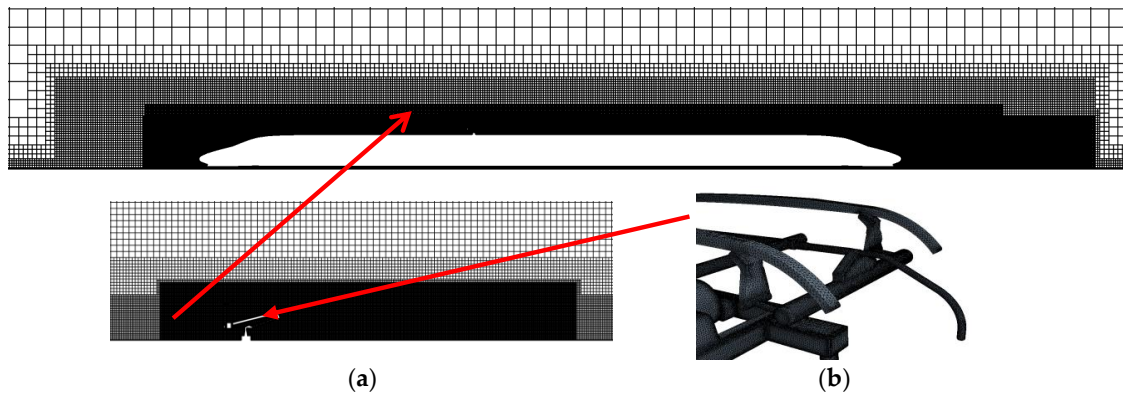


Figure 7. Medium sized computational mesh: (a) grid around pantograph; and (b) enlarged view of pantograph grid.

3.5. Validation of Computational Methods

Many structures of the pantograph could be treated as cylinders. The acoustic finite element method is first validated by a cylindrical flow calculation, as shown in Figure 8. The cylinder has a diameter of 10 mm, the length of the cylinder is πD , and the radius of the flow field is 15D. The trimmer meshing method is employed, and the first layer thickness is 0.0035 mm with a growth ratio of 1.1 in the wall-normal direction. The value of normalized wall-normal distance y^+ is defined as:

$$y^+ = \frac{u_* y}{\nu} \tag{10}$$

where y is the distance from the wall, u_* is the friction velocity ($u_* = (\frac{\tau_w}{\rho})^{1/2}$), τ_w is wall shear stress, ρ is the air density and ν is the air kinetic viscosity. The values of y^+ are below 1 in downstream of the front facing stagnation line on the cylinder surface, which is adequate for the LES model. The cylindrical surface grid size is 0.25 mm. The total number of cells is about 6 million. Figure 8 shows the boundary conditions, namely, the pressure far-field boundary with a uniform inlet velocity of 72 m/s and a gauge pressure of 0 Pa, and the parallel plane (on the two ends of a cylinder) is set as periodic.

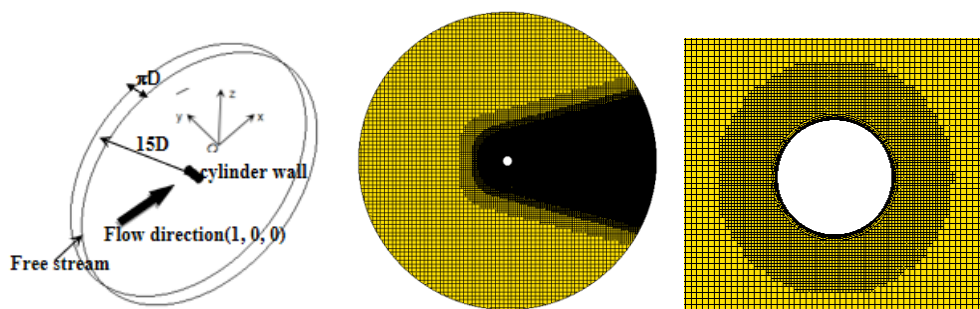


Figure 8. Circular cylinder model domain and discretization.

The LES method is used to calculate the flow field. The pressure–velocity coupling method is addressed by the Semi-Implicit Method for Pressure Linked Equations (SIMPLE) algorithm. The discrete algebraic equation is solved by the Gauss–Seidel iteration technique. Figure 9 shows the generation, development, and detachment of the leeward vortices downstream of the cylinder. The vortices alternate axially in the downstream direction of the flow, forming a von Karman vortex street. It can be seen that the leeward side vortices are mainly generated when the airflow flowing from the cylindrical wall surface leaves the leeward side wall surface. The generation, development and shedding of the vortices lead to noise generation. The acoustic FEM is used to solve the far-field noise at an inflow Mach number is 0.21. In this study, Kato equation [22] is used to correct the SPL obtained from numerical simulations because the spanwise length of the LES computational domain is limited by the available computational resources. As a result, the simulation spanwise length, L_{sim} , of the geometry is shorter than the experimental spanwise length, L_{exp} , reported in Jacob et al. [23]. To compare the predicted SPL with experimental data, the value obtained from numerical simulations must be corrected. The SPL is monitored 185D above directly the cylinder. Figure 10 shows the validations of the aerodynamic results and SPL results of 185D. It can be seen that the pressure coefficient (C_p) and the corresponding Strouhal number (St) of the vortex shedding predicted by the present study agrees with the experimental results and other numerical simulation solutions obtained in [23–26]. Therefore, it is reasonable to use the FEM for the far-field noise characteristic prediction in the following analysis.

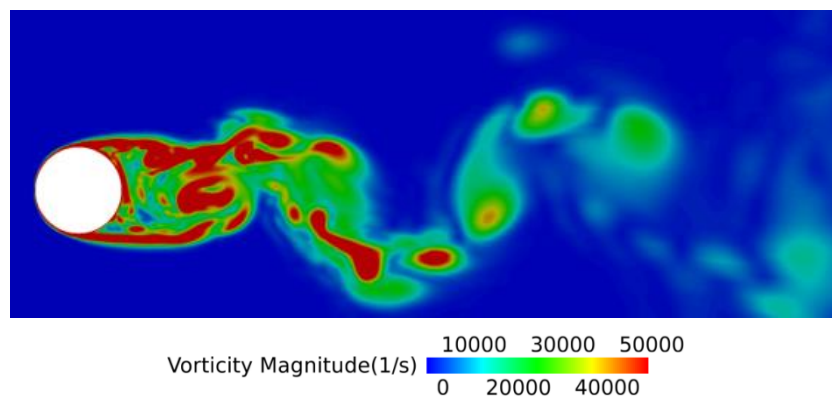


Figure 9. Vortex shedding on plane at 50% span(s^{-1}).

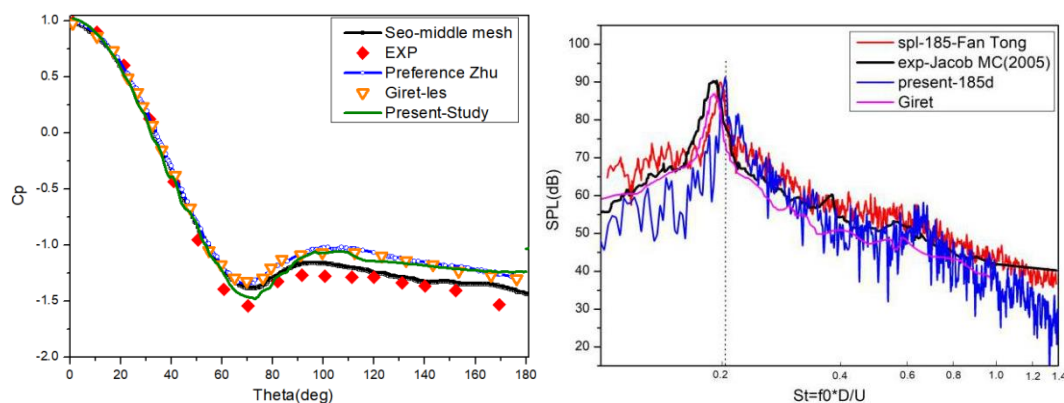


Figure 10. Validations of the C_p and SPL results at 185D (where $f_0 = 1508\text{Hz}$).

This paper seeks to show that the numerical method is able to model the evolution of the structures in the gap between the solid bodies. A comparison between downstream flow characteristics of the cylinder obtained by measurements and simulation using the same mesh level changes in the cylinder wake as used for the pantograph simulation is performed. As shown in Figure 11, the cylinder has a diameter of 0.05715 m, the separation distance, L , between the cylinders is $3.7D$. The length is $3D$.

The trimmer meshing method is employed, the first layer thickness is 0.001 mm with a growth ratio of 1.2 in the wall-normal direction. The cylindrical surface grid size is 1 mm. The total number of cells is about 8.5 million. The pressure outlet is set as a gauge pressure of 0 Pa, the inlet condition is set as a uniform velocity of 44 m/s, and the other parallel planes are given as symmetry.

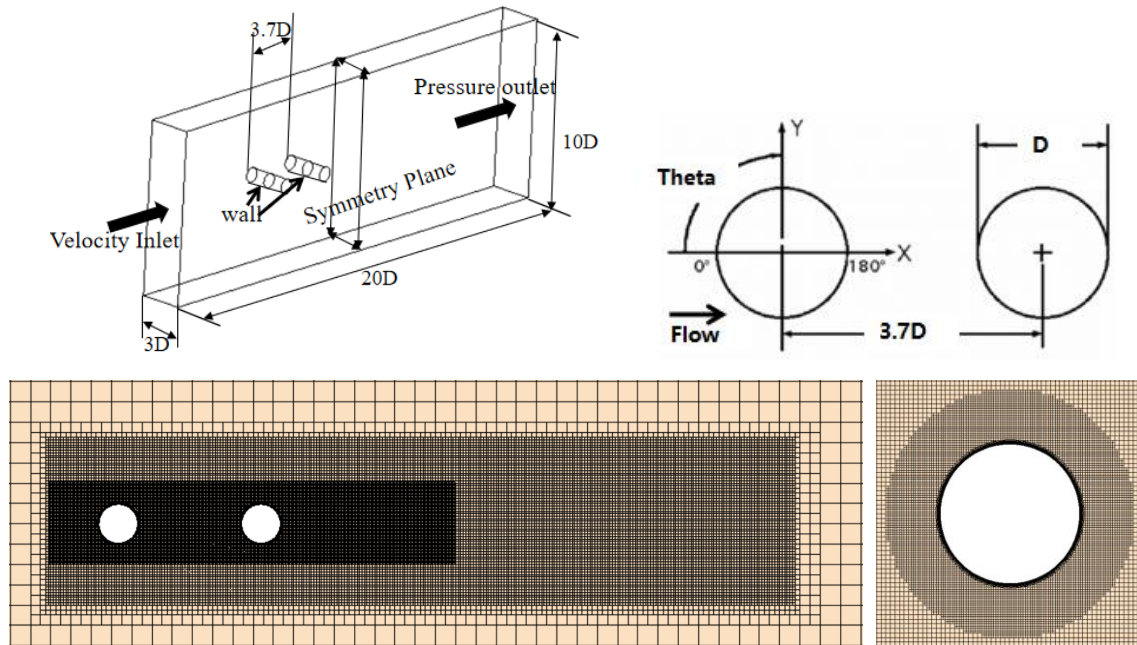


Figure 11. Geometry and computational domain for flow field of two cylinders in tandem.

Figure 12a shows the generation, development and detachment of the leeward vortices downstream of the two cylinders. The predicted root-mean-square (rms) of the pressure coefficient (C_p) on the cylinder downstream cylinder surfaces is compared with the previous work [27], in Figure 12b. The angle “Theta” is measured from the upstream stagnation point and is positive in the clockwise direction. The predicted results show that this method is suitable to obtain the flow characteristics in the gap and downstream between the solid bodies.

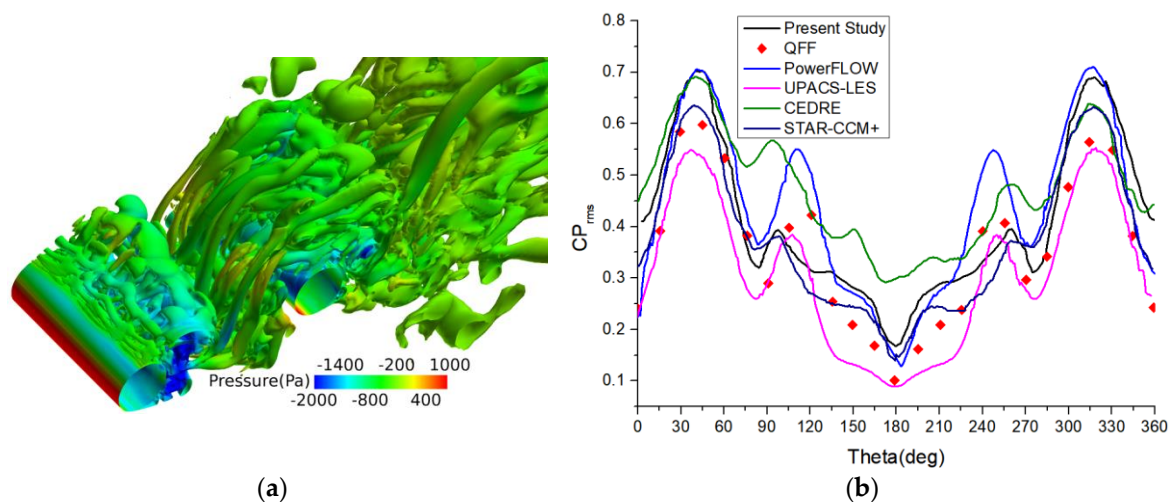


Figure 12. (a) Instantaneous iso-surface normalized Q-criterion ($Q = 100$); and (b) the root-mean-square (rms) of the perturbations in C_p .

4. Results and Discussion

4.1. Flow Characteristics of Pantograph Area

In this section, the flow characteristics around the pantograph and the installation bases are discussed. As shown in Figures 13 and 14, the vorticity and the instantaneous iso-surface vorticity as shown by the normalized Q-criterion, and the velocity streamlines around the pantograph are presented, respectively. In Figure 13, the flow separates over the pantograph surface. A series of vortices detaches from the leeward side of each rod and they interact with each other downstream. The hairpin vortices of different size are observed. In addition to the common characteristics of the flow field mentioned above, Figure 13a,b also shows that the flow field characteristics of the pantograph are different due to the opening directions of the pantograph. For the down-pantograph with flush installation base, the incoming flow first impacts on the corner of the upper and lower arm rods, and then strikes the rear of the carbon skateboard and the base in the downstream area. The turbulent upstream flow field hits downstream complex structure like the carbon skateboard and base again, which makes the flow field in the wake region more complex. Because the contact area between the pantograph and the incoming flow is concentrated, the eddy size under the larger contact area is also larger. For the up-pantograph, the distance between different structures on the pantograph is larger, and the inflow flows directly to the downstream area after impact with the carbon skateboard. Compared with the down-pantograph, the rear eddy scale is smaller. For Figure 13c, when the pantograph is placed in the cavity, the flow field above the cavity shielding part is almost the same as when it is installed on the flush surface. However, for the case that the pantograph is installed in the sunken base, the flow field characteristics have something in common with the general flow field in a cavity, as previously studied in [28–30]. However, the presence of the pantograph affects the pressure fluctuation on the cavity surface, and then it further affects the noise induced by the pantograph. For a pantograph that is installed in the sunken cavity, the base and insulator are basically located in the cavity, avoiding direct collision with the incoming flow. Generally, the flow past a cavity exhibits a strong relationship with the cavity length (L) to height (D) ratio as studied by Lawson and Barakos [19]. For the present study, the ratio of L/D of the cavity with pantograph is about 4.7. Therefore, according to the criterion of Lawson and Barakos [19], it is considered as the open cavity. In addition, the pressure field in the cavity is coupled with the shear layer shed from the cavity upstream edge, and the pressure fluctuation intensity in the cavity depends on the characteristics of the shear layer and on the evolution of momentum and vorticity during the impact of the shed shear layer with the cavity rear bulkhead as studied by Ouyang et al. [31]. Because the presence of the pantograph, the typical open cavity flow field structure is destroyed. As shown in Figure 14, one can observe that the air-flow acts on the pantograph first, and then vortices shed by the pantograph impinge on the surface downstream. A part of the air flow returns to the front of the cavity and continues to act on the pantograph. This differs from an empty cavity flow in which the shear layer shed at the cavity upstream edge impacts the cavity downstream edge, unobstructed. The pressure wave (feedback pressure wave) propagating upstream after acting on the surface of the cavity collides with the pressure wave reflected from the front wall when it arrives upstream at the last time. The air circulation inside and outside the cavity exchanges, resulting in pressure fluctuation in the cavity. The pressure fluctuation on the base and insulator surface even as well as the overall pressure fluctuation on the surface of the pantograph is affected by the flow in the cavity.

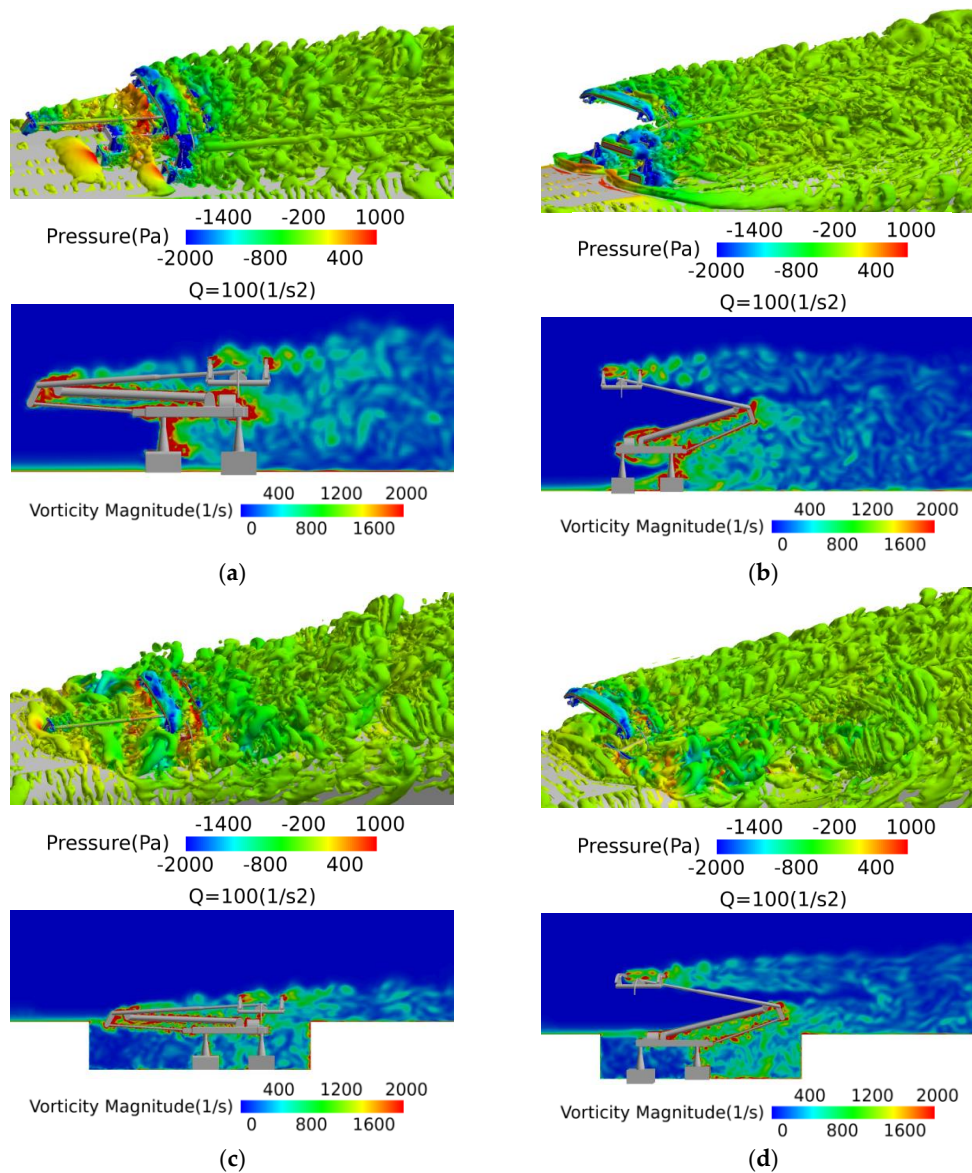


Figure 13. Instantaneous iso-surface normalized Q-criterion ($Q = 100/s^2$) and vorticity magnitude(1/s) on: (a) down-pantograph with flush base; (b) up-pantograph with flush base; (c) down-pantograph with sunken base; and (d) up-pantograph with sunken base.

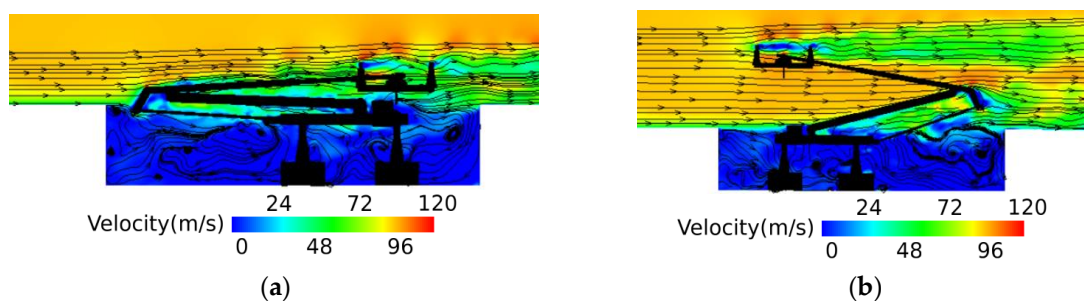


Figure 14. Streamlines superimposed on color iso-levels of the time-averaged velocity vector magnitude: (a) down-pantograph with sunken base; and (b) up-pantograph with sunken base.

4.2. Aerodynamic Noise Characteristics

4.2.1. Aerodynamic Noise Source

In this section, sources of aerodynamic noise are discussed as it is expected that the flow field of the different base configurations of the pantograph may have significant effects on noise spectrum characteristics and on the noise directivity, which could lead to a change in the perceived noise along the train track. Therefore, the aerodynamic pressure amplitude distributions on the pantograph at 200 Hz and 1000 Hz are compared. As shown in Figure 15, it can be observed that along the direction of the flow velocity, the aerodynamic pressure amplitude in the front regions of the pantograph is lower than that in the rear regions of the pantograph. This may be explained by the fact that the front parts always collide with the incoming flow sharply, forming a windward stagnation area. As a result, the fluctuating pressure is relatively small. Flow with higher levels of vorticity, as shown in Figure 13, passes over the rear parts of the pantograph. As a result, the amplitude of aerodynamic pressure fluctuation in the rear region is larger. Meanwhile, the amplitude of the aerodynamic pressure decreases when the frequency increases from 200 Hz to 1000 Hz. Where the flush configuration is used under the down-pantograph condition, the maximum aerodynamic pressure fluctuation at 1000 Hz is smaller than that at 200 Hz by as much as 18 dB. The phenomenon that the maximum aerodynamic pressure fluctuation decreases with the increasing frequency also can be observed by Zhang et al. [15]. At the low frequency, the SPL distribution of the aerodynamic pressure on the surface of the pantograph is non-uniform. The largest amplitude aerodynamic pressure mainly features on the supporting slide, the rotating shaft, the lower arm, and the leeward surface of the installation base. At 1000 Hz, the aerodynamic pressure amplitude distribution is more uniform than that at 200 Hz. It seems that, although the aerodynamic pressure amplitude distribution over the pantograph surfaces are different at these two frequencies, the largest amplitudes are always located on the downstream base frame, the connection between the upper and lower arms and the downstream position of the double skateboard bow. These aerodynamic pressure fluctuations act as dipole noise sources.

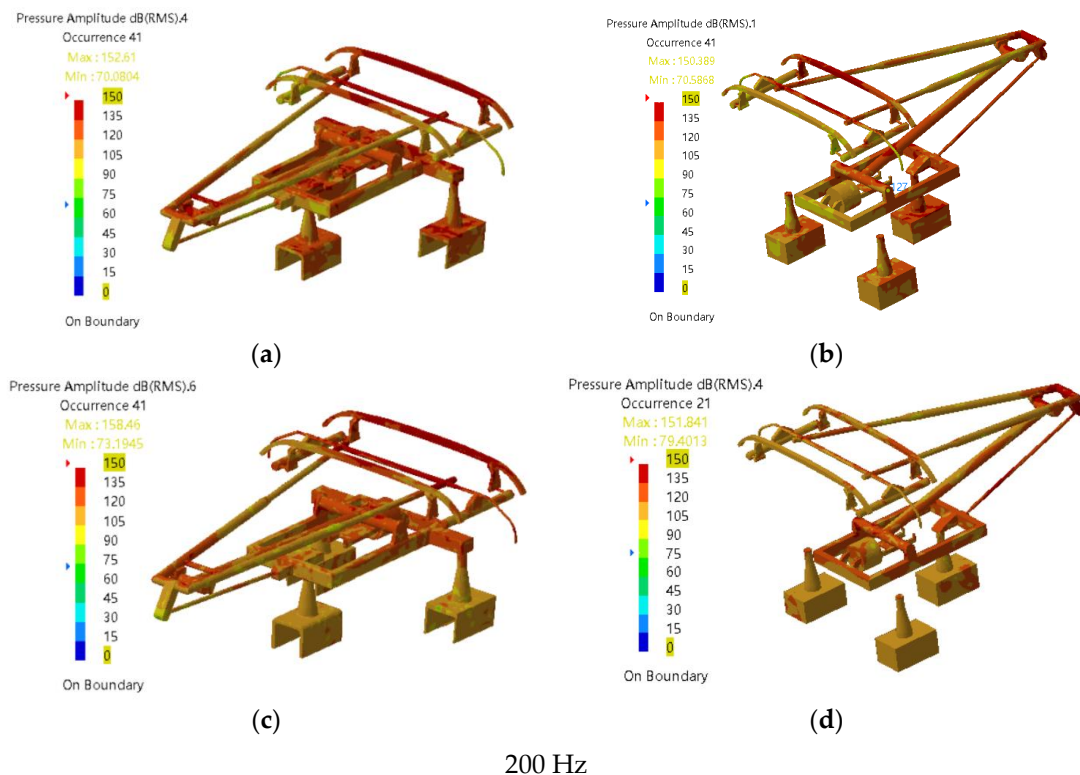


Figure 15. Cont.

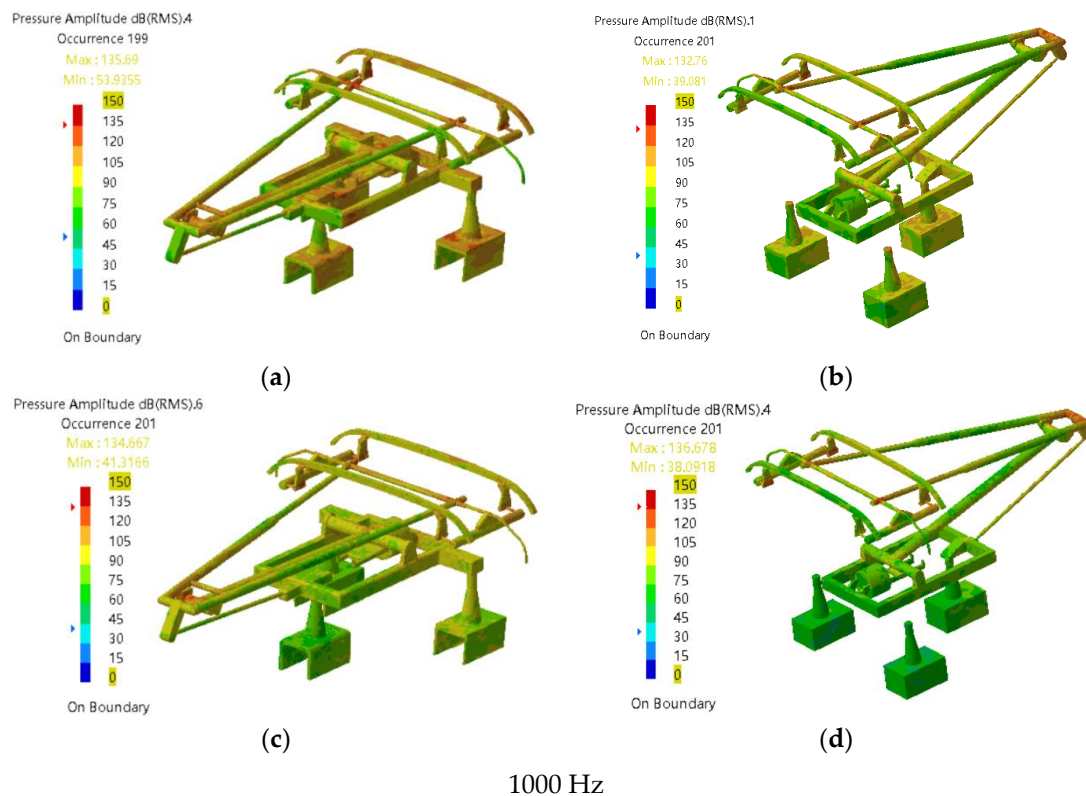


Figure 15. Normalized aerodynamic pressure fluctuation amplitude at 200 and 1000 Hz on: (a) down-pantograph with flush base; (b) up-pantograph with flush base; (c) down-pantograph with sunken base; and (d) up-pantograph with sunken base.

4.2.2. Aerodynamic Noise Radiation and Attenuation Characteristics

To study aerodynamic noise radiation and attenuation characteristics induced by the up- and down-pantograph with the different base configurations, the contours of spatial distribution in near-field and far-field noise at three planes in the y -direction i.e. $y = 0$ (near-field), 10 and 20 m (in far-field) are compared, as depicted in Figure 16. In this analysis, the acoustic finite element method is directly used to deal with the whole field noise, including near-field $y = 0$ plane noise, without considering the effect of quadrupole noise and corresponding convection effect. The main reason is that Mach number of the incoming flow is only 0.278 in this calculation. As it is known that the ratio of quadrupole noise to dipole noise is proportional to the square of Mach number [32], the influence of the quadrupole noise at this speed is relatively small, and it is reasonable to ignore it in the present study. As the pantograph is the noise source, the sound pressure decreases with the y distance. The contours also indicate that the regions with higher sound levels for both frequencies are in the vicinity of the pantograph. These distributions are more uniform at the high frequency. It is shown that, as frequency increases, the sound pressure amplitude decreases.

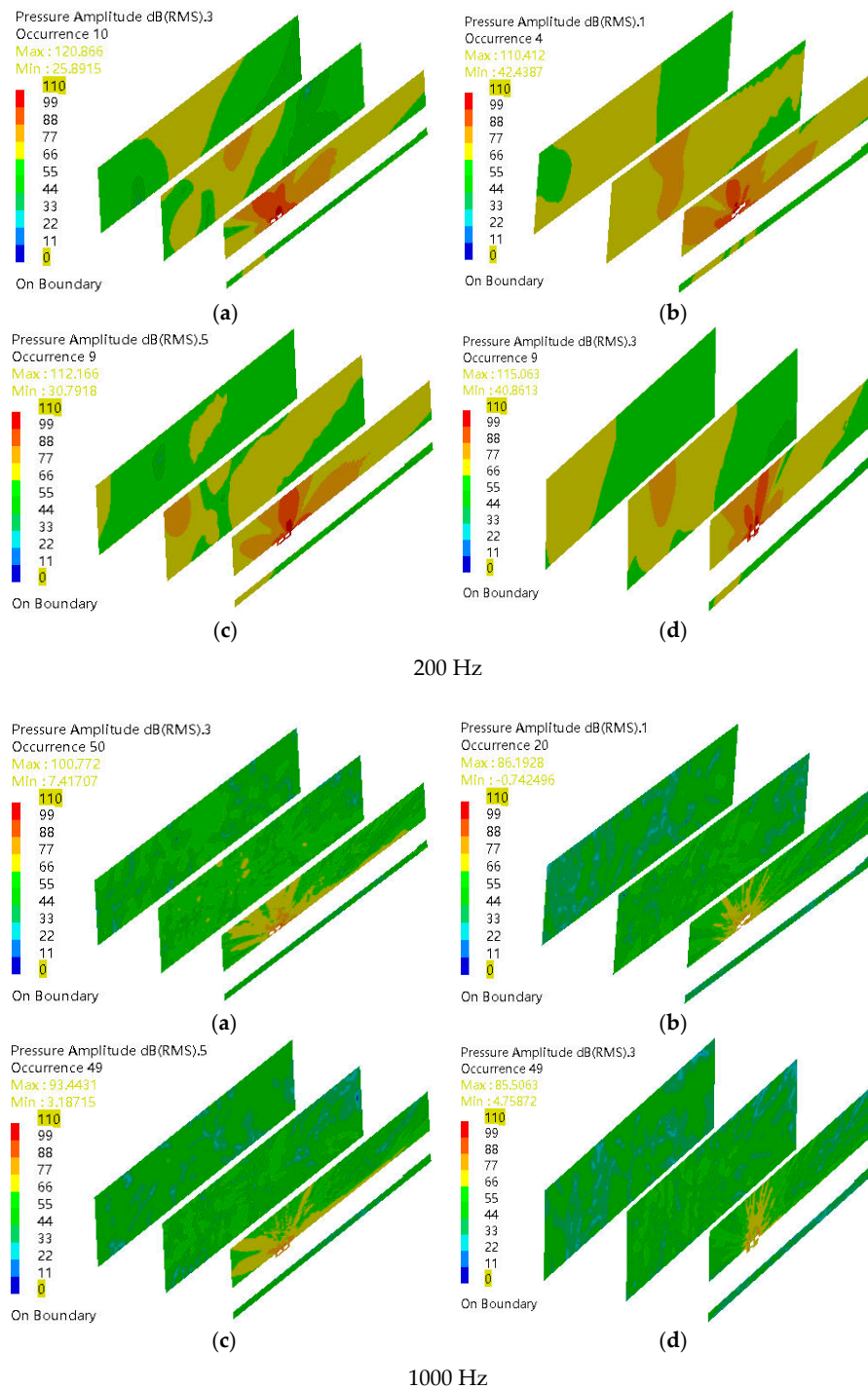


Figure 16. Spatial distribution of near-field ($Y = 0$ m) and far-field ($Y = 10$ m, $Y = 20$ m) noise at 200 Hz and 1000 Hz on: (a) down-pantograph with flush base; (b) up-pantograph with flush base; (c) down-pantograph with sunken base; and (d) up-pantograph with sunken base.

To obtain the noise characteristics in the far field, two positions in the y -direction, i.e. at $y = 5$ m and $y = 25$ m from the center line of the train, as shown previously in Figure 4, are evaluated, as plotted in Figure 17. Some phenomena are observed. Firstly, the noise amplitude at $y = 25$ m is lower than that at $y = 5$ m at all frequencies. Next, it is shown that the noise caused by the down-pantograph is higher than that by the up-pantograph. Finally, the noise from the pantograph with the flush base configuration is of higher amplitude than that with the sunken base configuration irrespective of

whether the pantograph is under the up or down condition. These phenomena could be explained by the fact that, for the sunken configuration, the vortices generated in the rear of the insulator and the base move inside the cavity and the movement to the surroundings is blocked by the cavity surface. This may explain the predicted weakening of the far-field noise. Additionally, one can see that, for frequencies below 200 Hz, the noise caused by the sunken type configuration is almost the same as that from the flush. However, at higher frequencies, the noise caused by the sunken configuration of the pantograph is lower than that by the flush configuration in general. This is because the large vortices produced by the sunken insulator are blocked by the cavity, therefore their streamwise growth and spread are constrained. As a result, large eddies are not easily broken into small ones.

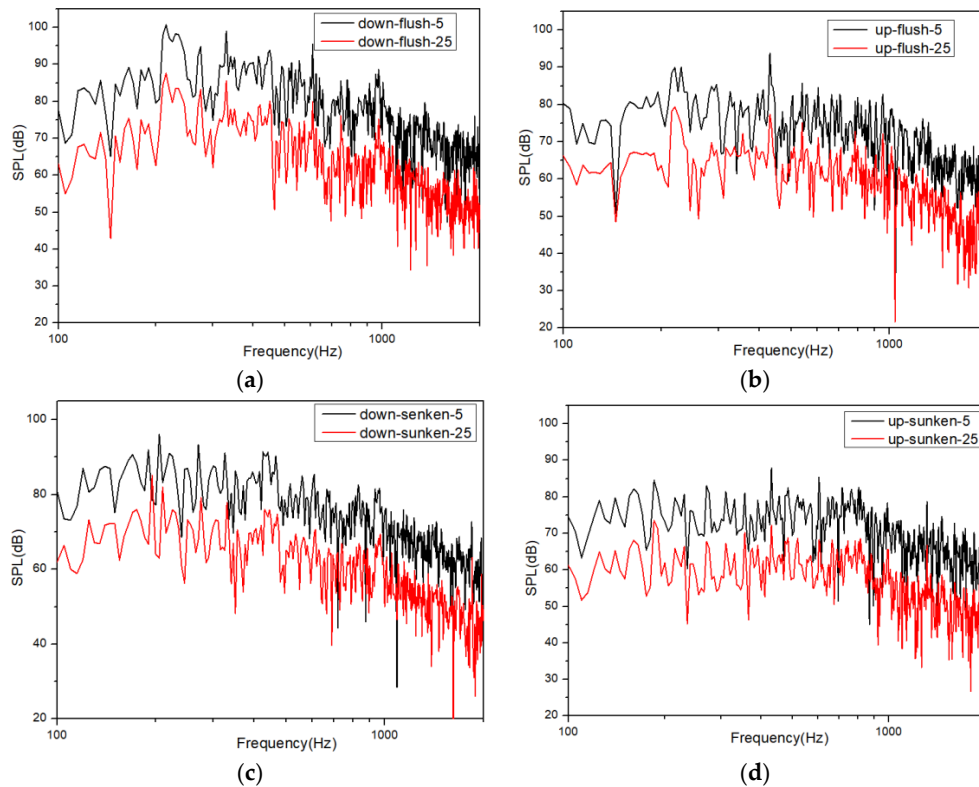


Figure 17. Noise predictions at the far field monitoring points. (a) Noise of down-pantograph with flush base; (b) Noise of up-pantograph with flush base; (c) Noise of down-pantograph with sunken base; and (d) Noise of up-pantograph with sunken base.

To further study the trend of the overall sound pressure levels (OASPL) at different distances along x (parallel to the train) and y (normal to the train) directions, Figure 18a,b shows the OASPL in the far field along the x and y directions, respectively. Figure 18a indicates that the OASPL is inversely proportional to the distance of sound source for all cases. To predict the OASPL in the region from the pantograph to the far field, it is found that the logarithm function, $OASPL = OASPL_0 - b \times \ln(x + c)$, is fitted appropriately using the values of the OASPL under the relation between the OASPL and the distance in the range of $0 \leq y \leq 30$ m. The four correlations obtained by the fitted curves are mathematically expressed as follows: (1) $OASPL = 107.3 - 8.9 \times \ln(x - 0.50)$ for the down-pantograph with the flush base; (2) $OASPL = 105.5 - 8.8 \times \ln(x - 0.03)$ for the up-pantograph with the flush base; (3) $OASPL = 102.9 - 9.1 \times \ln(x - 0.12)$ for the down-pantograph with the sunken base; and (4) $OASPL = 97.1 - 7.9 \times \ln(x - 0.46)$ for the up-pantograph with the sunken base. Another observation is that the differences between the OASPL obtained by the up- and down-pantograph with the flush configuration base at each position are about 1–2 dB, whereas the differences between the OASPL obtained by the up- and down-pantograph with the sunken base at each position are about 4–5 dB. Besides, under the same configuration base, the OASPL obtained by the down-pantograph is higher

than that by the up-pantograph. To evaluate the OASPL caused by the pantograph in the far-field region, it is acceptable if the distance from the sound source is more than 25 m, the sound source is assumed as a point source [13]. Therefore, the sound pressure propagation can be considered as the spherical surface from the point source center and the attenuation value ΔL of the OASPL from the point source in the far-field regions is computed by the equation: $\Delta L = 20\log(r/r_0)$. This can be used to predict the geometric attenuation of noise. Figure 18b shows the OASPL along the x direction at $y = 25$ m. The down-pantograph always produces higher noise than the up-pantograph for both configuration bases. Besides, Figure 18a,b indicates that the OASPL in the far field along the x and y directions are always found that for all x and y positions the down-pantograph with the flush base provides the highest OASPL. The lowest OASPL is obtained by the up-pantograph with the sunken base. In addition, the OASPL caused by the up-pantograph with the flush base is higher than that by the down-pantograph with the sunken base.

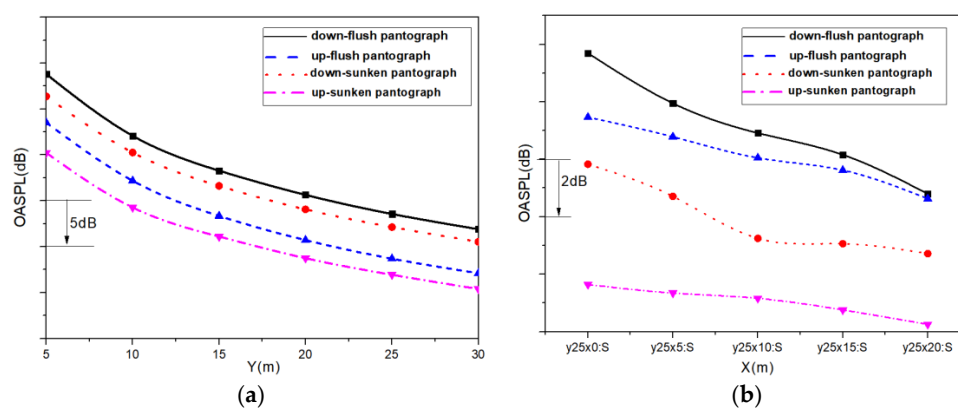


Figure 18. Comparison of OASPL at different distances of pantographs with different configuration bases: (a) with pantograph as reference position, OASPL at different vertical distances from center line of track in horizontal plane; and (b) OASPL of up- and down-pantograph with different configuration bases at different monitoring points along moving direction of train.

4.2.3. Aerodynamic Noise Directivity

In this section, the aerodynamic noise directivity around the pantograph with the different configurations is presented. According to the ISO3095-2013 standard [33], the far-field noise receivers should be located 7.5 or 25 m away from the center line of the track and 1.2 or 3.5 m above the ground. The present study investigates the far-field noise characteristics around the pantograph with a distance of 7.5 m in the radial direction and 3.5 m above the ground. The OASPL in the X-Y, Y-Z and X-Z planes is discussed, as shown in Figure 19, and the OASPL is considered at every five degrees. It is found that in all the planes the noise directivity induced by the sunken pantograph is slightly smaller than the flush pantograph in general. Only at some angles, the noise induced by the sunken pantograph is equal to or larger than that by the flush pantograph. Besides, some interesting phenomena are observed in each plane. First, in the X-Y plane, when the pantograph is used with the flush surface, a relatively high OASPL is found in the rear arc of the pantograph ($-5^\circ \leq \theta \leq 5^\circ$), and along the sideline over the ranges $85^\circ \leq \theta \leq 125^\circ$ and $235^\circ \leq \theta \leq 275^\circ$. When the pantograph is installed in the sunken surface, the rear arc still has the higher OASPL. However, the high OASPL values are also predicted at other angles. In the down-pantograph, a large part of the structure is located inside the cavity. The corresponding amplitude of the four corners of the cavity is slightly higher than that of other positions. This may be because of the effects of the sunken configuration. Specifically, during the process of noise propagation, the sound wave can reflect within the cavity of the sunken surface, four corners can easily become the convergence area of reflected sound waves. One can see that the directivity of noise is not completely symmetrical the X-Y plane. Similar instances of incomplete symmetry are also reported in the literature [13]. The main reason is that the far-field noise monitors are usually placed at

every 5–10 degrees around the pantograph in different planes. This may omit part of the amplitude between the monitors, resulting a certain impact on the results. In addition, in the calculation of the sound field, the frequency resolution has a slight impact on the results. However, further detailed analysis of the up- and down-pantograph in the cavity has shown that there is almost no difference when the frequency resolution is increased from 10 Hz to 5 Hz, namely, the overall noise difference is less than 1 dB. In the Y-Z plane, the noise distributions obtained by the two installation bases are nearly symmetric and the higher sound level area is found in in the range of $60^\circ \leq \theta \leq 120^\circ$. It also shows that, in this range of theta with the pantograph under the down configuration, the OASPL obtained by the flush installation base is higher than that by the sunken base configuration. However, under the up-pantograph condition, the OASPL values obtained by the two configuration bases are close to each other. In the X-Z plane, the down-pantograph with the flush base produces higher noise than the sunken base in all directions. For the up-pantograph, the noise amplitudes of the flush and sunken bases are very close to each other in general. Nonetheless, it is seen that at some angles, the noise induced by the sunken base is higher than the flush base. In both Y-Z and X-Z plane, for the up-pantograph with the flush base or sunken base, it can be seen that the noise amplitudes are very close to each other in general, especially in the Z direction directly above the body. This may be due to the effect of sound wave reflection from the cavity floor and that the up-pantograph itself is a large source of noise in this direction.

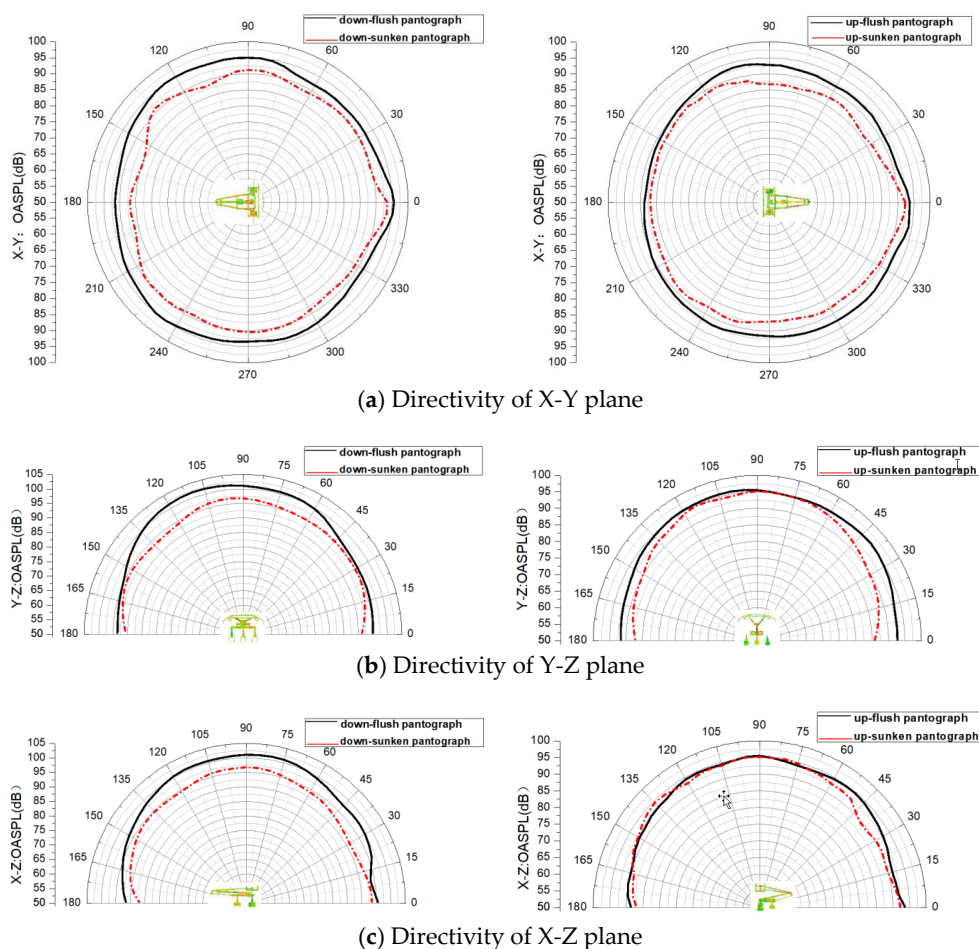


Figure 19. Noise directivity induced by pantograph in different planes (the left side figures show the down condition and the right side figures show the up condition): (a) directivity of X-Y plane; (b) directivity of Y-Z plane; and (c) directivity of X-Z plane.

5. Conclusions

This work presents the numerical study of the aerodynamic noise characteristics induced by a pantograph over a simplified train geometry with the different configurations of the installation base using the large eddy simulation (LES) with finite element method (FEM). The numerical results are carried out in terms of the flow field around the pantograph and its installation base, the spatial distribution and spectrum characteristics, and the noise directivity in near and far fields under the up and down conditions at the train speed of 350 km/h. Through the discussion, the following interesting phenomena are drawn:

(1) The complex shape of the pantograph is the main reason for its induced aerodynamic noise. A series of vortices detaches from the leeward side of each rod and they interact with each other and with downstream solid structures. The aerodynamic pressure fluctuation is generated on the rods induces aerodynamic noise. The main aerodynamic noise sources are located on the downstream base frame and on the double skateboard bow, at the connection between the upper and lower arms. The aerodynamic noise sources over the pantograph surfaces are different at 200 Hz and at 1 kHz.

(2) For the spatial distributions, along the direction of the flow velocity, the aerodynamic pressure fluctuation amplitude in the front regions of the pantograph is lower than that in the rear regions of the pantograph. These distributions are more uniform at 1 kHz than at 200 Hz. In addition, the amplitude of the noise is lower at the higher frequency.

(3) In the far-field regions along the x and y directions, for all x and y positions under the pantograph shape and opening direction selected in this paper, the down-pantograph with the flush configuration provides the highest OASPL. The up-pantograph with the sunken configuration produces the lowest OASPL. In addition, the OASPL caused by the up-pantograph with the flush base is higher than that by the down-pantograph with the sunken base. Thus, the pantograph with sunken configuration is a better choice in a practical engineering application.

(4) On the directivity, the noise induced by the pantograph with the sunken surface is of lower amplitude than that with the flush surface, especially in the down-pantograph. For up-pantograph, the amplitude of the noise from the sunken surface configuration is close to that from the flush surface configuration in Y - Z plane and in the X - Z plane. In the X - Z plane, the results even show noise amplitude from the sunken surface configuration is predicted to be higher than that from the flush configurations at some angles in some angles. However, this still does not affect the fact that the sunken installation is conducive to a quieter noise environment on both sides of the road.

It should be noted that effects of noise transmission to the exterior and interior of high-speed train need to be further studied, especially in the case of the pantograph with the sunken configuration. The present study considers only the aerodynamic noise generated by the wall fluctuating pressure of the pantograph in the exterior noise transmission to the environment. In fact, there are strong vortices in the regions near the pantograph and spatial distribution of near-field, such as $Y = 0$ m, may obtain a more accurate result. These are the quadrupole noise sources that contribute to aerodynamic noise. Since the operating speed is not too high ($Ma = 0.278$), the proportion of noise generated by the quadrupole source, which scales by u^8 [34], is smaller than that from dipole sources, which scales as u^6 [35], where u is the train velocity. Thus, the induced noise by the quadrupole source is not included in this study.

Author Contributions: Conceptualization, Z.S. and G.Y.; Data curation, Y.Y.; Formal analysis, Y.Y.; Funding acquisition, Z.S. and G.Y.; Investigation, Y.Y. and Z.S.; Methodology, Y.Y. and W.L.; Project administration, Z.S. and G.Y.; Resources, Z.S. and G.Y.; Software, Y.Y. and W.L.; Supervision, Z.S. and G.Y.; Validation, Y.Y. and Z.S.; Visualization, Y.Y.; Writing—original draft, Y.Y.; and Writing—review and editing, Y.Y., P.P., and Z.S.

Funding: This research is funded by Advanced Rail Transportation Special Plan in National Key Research and Development Project, grant number 2016YFB1200601-B13 and 2016YFB1200602-09.

Acknowledgments: The author would like to gratefully acknowledge the Computing Facility for the “Era” petascale supercomputer of Computer Network Information Center of Chinese Academy of Sciences. The first author would like to thank University of Chinese Academy of Sciences and Institute of Mechanics under Chinese Academy of Sciences for all support.

Conflicts of Interest: The authors declare no conflict of interest.

References

1. Zhang, S.G. Noise mechanism, sound source identification and control of high-speed train in the speed of 350 km·h⁻¹. *Chin. Railw. Sci.* **2009**, *30*, 86–90. (In Chinese) [[CrossRef](#)]
2. Lele, S.K. Compact finite difference schemes with spectral-like resolution. *J. Comput. Phys.* **1992**, *103*, 16–42. [[CrossRef](#)]
3. Sun, Z.X.; Song, J.J.; An, Y.R. Numerical simulation of aerodynamic noise generated by crh3 high speed train. *J. Peking Univ.* **2012**, *48*, 701–711. (In Chinese)
4. Liu, J.L.; Zhang, J.Y.; Zhang, W.H. Numerical analysis of aerodynamic noise of high-speed train head. *J. Railw.* **2011**, *9*, 19–26. (In Chinese)
5. Zhu, J.Y.; Jing, J.H. Research and control of aerodynamic noise in high speed trains. *Foreign Railw. Cars* **2011**, *48*, 1–8. (In Chinese)
6. Sun, Y.J.; Xia, J.; Mei, Y.G. Introduction of aerodynamic noise generated by high-speed train and the reduction of the noise. *Railw. Locomot. Car* **2009**, *29*, 25–28. (In Chinese)
7. King, W.F. A precise of development in the aeroacoustics of fast trains. *J. Sound Vib.* **1996**, *193*, 349–358. [[CrossRef](#)]
8. Takaishi, T.; Ikeda, M. Method of evaluating dipole sound source in a finite computational domain. *Railw. Tech. Res. Inst.* **2004**, *116*, 1427–1435. [[CrossRef](#)]
9. Takaishi, T.; Sagawa, A.; Nagakura, K.; Maeda, T. Numerical analysis of dipole sound source around high-speed trains. *Railw. Tech. Res. Inst.* **2002**, *111*, 2601–2608.
10. Yoshiki, K.; Yusuke, W.; Fumio, M. Numerical simulation of aerodynamic noise from high-speed pantographs using lattice Boltzmann method. In Proceedings of the International Symposium on Speed-Up, Safety and Service Technology for Railway and Maglev Systems, Seoul, Korea, 17–19 September 2012; pp. 1–9.
11. Liu, J.L.; Yu, M.G.; Tian, A.Q. Study on the aerodynamic noise characteristics of the pantograph of the high-speed train. *J. Mech. Eng.* **2018**, *54*. [[CrossRef](#)]
12. Tan, X.M.; Xie, P.P. Vortex structures and aeroacoustic performance of the flow field of the pantograph. *Sound Vib.* **2018**, *432*, 17–32.
13. Yu, H.H.; Li, J.C.; Zhang, H.Q. On aerodynamic noises radiated by the pantograph system of high-speed trains. *Acta Mech. Sin.* **2013**, *29*, 399–410. [[CrossRef](#)]
14. Sun, X.Q.; Xiao, H. Numerical modeling and investigation on aerodynamic noise characteristics of pantographs in high-speed trains. *Complexity* **2018**, *2018*, 1–12. [[CrossRef](#)]
15. Zhang, Y.D.; Zhang, J.Y.; Li, T.; Zhang, L. Investigation of the aeroacoustic behavior and aerodynamic noise of a high-speed train pantograph. *Technol. Sci.* **2017**, *60*, 561–575. [[CrossRef](#)]
16. Kitagawa, T.; Nagakura, K. Aerodynamic noise generated by shinkansen cars. *J. Sound Vib.* **2000**, *231*, 913–924. [[CrossRef](#)]
17. Nagakura, K. Localization of aerodynamic noise sources of shinkansen train. *J. Sound Vib.* **2006**, *293*, 547–556. [[CrossRef](#)]
18. Noger, C.; Patrat, J.C.; Peube, J. Aeroacoustical study of the TGV pantograph research. *J. Sound Vib.* **2000**, *231*, 563–575. [[CrossRef](#)]
19. Lawson, S.J.; Barakos, G.N. Review of numerical simulations for high-speed, turbulent cavity flows. *Prog. Aerosp. Sci.* **2011**, *47*, 186–216. [[CrossRef](#)]
20. Smagorinsky, J. General circulation experiments with the primitive equations. *Basic Exp.* **1963**, *93*, 99–165. [[CrossRef](#)]
21. Fioravanti, A.; Lenzi, G.; Ferrara, G.; Vichi, G.; Ricci, S.; Bagnoli, L. Assessment and experimental validation of a 3D acoustic model of a motorcycle muffler SAE. *Int. J. Eng.* **2015**, *8*, 266–276.
22. Kato, C.; Lida, A.; Fujita, H.; Ikegawa, M. Numerical prediction of aerodynamic noise from low Mach number turbulent wake. In Proceedings of the AIAA 93-0145, 31st Aerospace Sciences Meeting & Exhibit, Reno, NV, USA, 11–14 January 1993.
23. Jacob, M.C.; Boudet, J.; Casalino, D.; Michard, M. A rod-airfoil experiment as benchmark for broadband noise. *Theor. Comput. Fluid Dyn.* **2005**, *19*, 171–196. [[CrossRef](#)]

24. Giret, J.C.; Sengissen, A.; Moreau, S.; Sanjosé, M.; Jouhaud, J.C. Prediction of the sound generated by a rod-airfoil configuration using a compressible unstructured LES solver and a FW-H analogy. In Proceedings of the 18th AIAA/CEAS aeroacoustics conference, Colorado Springs, CO, USA, 4–6 June 2012; pp. 2012–2058.
25. Fan, T.; Qiao, W.Y.; Chen, W.J.; Wang, L.F.; Wang, X.N. Broadband noise prediction using large eddy simulation and a frequency domain method. *Appl. Acoust.* **2017**, *117*, 94–105.
26. Zhu, W.Q.; Luo, K.Y.; Xiao, Z.X. Numerical simulations of the flow dynamics past an oscillating rod-airfoil configuration. In *Symposium on Hybrid RANS-LES Methods*; Springer: Cham, Switzerland, 2016; pp. 433–443.
27. Lockard, D.P. Summary of the tandem cylinder solutions from the benchmark problems for airframe noise computations—Workshop. In Proceedings of the 49th AIAA Aerospace Sciences Meeting including the New Horizons Forum and Aerospace Exposition, Orlando, FL, USA, 4–7 January 2011.
28. Plentovich, E.B.; Stallings, J.R.L.; Tracy, M.B. *Experimental Cavity Pressure Measurements at Subsonic and Transonic Speeds. Static-Pressure Results*; Nasa Technical Paper; NASA Langley Research Center: Hampton, VA, USA, 1994; pp. 687–714.
29. Ukeiley, L.; Murray, N. Velocity and surface pressure measurements in an open cavity. *Exp. Fluids* **2005**, *38*, 656–671. [[CrossRef](#)]
30. Sinha, N.; Arunajatesan, S.; Shipman, J. High fidelity simulation and measurements of aircraft weapons bay dynamics. In Proceedings of the 7th AIAA/CEAS Aeroacoustics Conference and Exhibit, Berlin, Germany, 27–29 May 2013; pp. 6331–6335.
31. Ouyang, S.X.; Liu, X.Q.; Zhang, B.B. Cavity Flow Simulation and Noise Analysis Using DES Method. *J. Nanjing Univ. Aeronaut. Astronaut.* **2012**, *44*, 6.
32. Xiao, Y.G.; Kang, Z.C. Numerical prediction of aerodynamic noise radiated from high speed train head surface. *J. Cent. South Univ.* **2008**, *39*, 6.
33. European Committee for Standardization. *ISO 3095: 2013 Railway Application Acoustics Measurement of Noise Emitted by Railbound Vehicles*; British Standards Institution: London, UK, 2013.
34. Lighthill, M.J. On sound generated aerodynamically I. General Theory. *Proc. R. Soc. Lond. A* **1952**, *211*, 564–587.
35. Curle, N. The influence of solid boundaries upon aerodynamic sound. *Proc. R. Soc. Lond. Ser. A Math. Phys. Eng. Sci.* **1955**, *231*, 505–514.



© 2019 by the authors. Licensee MDPI, Basel, Switzerland. This article is an open access article distributed under the terms and conditions of the Creative Commons Attribution (CC BY) license (<http://creativecommons.org/licenses/by/4.0/>).